Journal of
*Marine Science and Engineering*

MDPI

*Article*

# Multiple Controls on Organic Matter Accumulation in the Intraplatform Basin of the Early Cambrian Yangtze Platform, South China

**Qiyang Zhang [1], Entao Liu [1,*], Songqi Pan [2], Hua Wang [1,*], Zhenhua Jing [2], Zhengfu Zhao [2] and Ruiyue Zhu [1]**

[1] Key Laboratory of Tectonics and Petroleum Resources of Ministry of Education, China University of Geosciences, Wuhan 430074, China; zhangqiyang@cug.edu.cn (Q.Z.); ruiyue.zhu@cug.edu.cn (R.Z.)
[2] Sinopec Petroleum Exploration and Production Research Institute, Beijing 100083, China; pansongqi@pku.edu.cn (S.P.); z.jing@pku.edu.cn (Z.J.); zhao_zhengfu@pku.edu.cn (Z.Z.)
* Correspondence: liuentao@cug.edu.cn (E.L.); wanghua@cug.edu.cn (H.W.)

**Abstract:** Studying the accumulation rules of organic matter (OM) in paleo-ocean sediments can not only enhance our understanding of how OM becomes enriched in ancient oceans but also provide guidance for the exploration of shale gas in unconventional shale strata. A breakthrough has been made in shale gas exploration in the early Cambrian Qiongzhusi Formation in South China. However, less attention has been paid to the intraplatform basin of the Yangtze Platform, and the factors controlling organic matter enrichment in this special region remain unclear. This study focuses on a continuous drilling core across the full well section of the Qiongzhusi Formation in the intraplatform basin of the Yangtze Platform. Through the comprehensive analysis of total organic carbon (TOC), major and trace elements, and Mo isotopes, this study investigates the controlling factors for OM enrichment with $\delta^{98/95}$Mo ratios utilized to identify the existence of euxinic bottom water. The examined 240 m long core can be divided into four units, where the TOC values of the lower Units 1 and 2 (0.2–5.0 wt.%) average higher than the upper Units 3 and 4 (0.2–2.5 wt.%). Redox indicators (U/Th, Ni/Co, EF(Mo)—EF(U)) indicate an increasing oxidation of bottom waters from the bottom upwards. $\delta^{98/95}$Mo data further confirm the presence of weakly euxinic conditions in Units 1 and 2, addressing the ongoing controversy surrounding bottom water redox environments. Primary productivity indicators (Ni/Al, Cu/Al) suggest a relatively low average productivity level within the intraplatform basin. The upwelling indicators EF(Co) * EF(Mn) of different profiles in the Yangtze Platform suggest that low productivity within the intraplatform basin can be mainly attributed to the absence of upwelling. Consequently, this study proposes an organic matter enrichment mechanism for the Qiongzhusi Formation in the intraplatform basin, which emphasizes the significance of the redox environment in the formation of high-quality hydrocarbon source rocks in restricted environments that lack upwelling, setting it apart from the deep ocean. These findings have the potential to provide valuable insights for the exploration of high-quality hydrocarbon source rocks in other similar regions.

**Keywords:** organic matter; redox conditions; primary productivity; lower Cambrian; Sichuan Basin



**Citation:** Zhang, Q.; Liu, E.; Pan, S.; Wang, H.; Jing, Z.; Zhao, Z.; Zhu, R. Multiple Controls on Organic Matter Accumulation in the Intraplatform Basin of the Early Cambrian Yangtze Platform, South China. *J. Mar. Sci. Eng.* **2023**, *11*, 1907. https://doi.org/10.3390/jmse11101907

Academic Editor: George Kontakiotis

Received: 4 September 2023
Revised: 28 September 2023
Accepted: 29 September 2023
Published: 2 October 2023



## 1. Introduction

Significant biological, oceanographic, and geochemical changes occurred during the Ediacaran–Cambrian (E–C) transition [1–6]. Serving as a key record of this interval, lower Cambrian black shales contain valuable information about the marine environment and the evolution of life [7–9]. There are two main modes of organic matter (OM) accumulation: a preservation mode primarily controlled by redox conditions [10,11], with the modern Black Sea being a typical example, and a productivity mode primarily influenced by high productivity [12], such as the modern Arabian Sea. The organic matter enrichment

of marine shale is affected by high palaeoproductivity and anoxic environment [13–16]. Additionally, some studies emphasize that OM enrichment is also influenced by factors like water mass restrictions, circulation pattern changes, and terrigenous input [11,17–21]. Recently, an increasing number of studies suggest that the enrichment of OM in shale is likely controlled by multiple factors, including productivity and redox conditions, with potentially different controlling processes in different environmental types [15,20–23].

During the Early Cambrian, widespread deposition of lower Cambrian Qiongzhusi Formation black shale occurred on the Yangtze Block under global sea level rise and transgression [24,25]. During this interval, the Yangtze Block developed various depositional environments, including deep-water slope and basinal facies, transitional facies, carbonate platform facies, and an intraplatform basin [7,26,27] (Figure 1a). Previous studies based on profile sampling and drilling analysis have revealed sea level fluctuations and upwelling events occurring in deep-water slope and basinal facies and carbonate platform facies. These events further influenced the OM enrichment through modifying water column redox conditions and primary productivity within the region [20,28–32]. However, compared to other well-investigated regions of the Yangtze Block [23,33,34], whether the upwelling existed in the region of the intraplatform basin is still unclear.

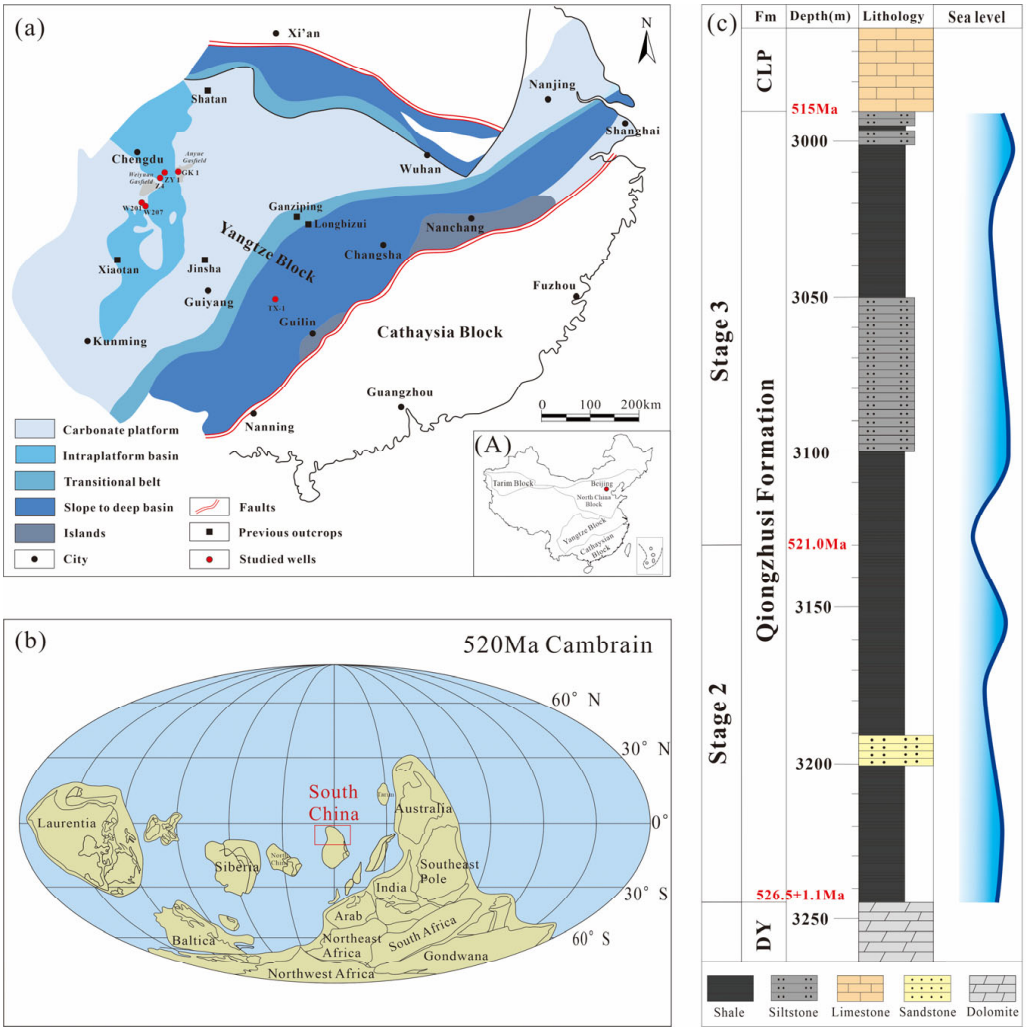


**Figure 1.** (**a**) Paleogeographic map of the Yangtze Block during the Ediacaran–early Cambrian transition (modified form the References [20,23,24]); (**b**) Early Cambrian global paleogeography (modified form the References [35,36]); (**c**) Stratigraphic column of the Qiongzhusi Formation in the W207 well (the relative sea level changes are modified from Reference [36]).

The facies of the intraplatform basin represent a favorable accumulation zone for high-quality hydrocarbon source rocks during the Early Cambrian [20], with the Anyue and Weiyuan Gas Fields discovered on the two sides [37] (Figure 1a), and possess high hydrocarbon recovery [38]. Compared to the other structural units (e.g., slope to deep ocean and carbonate platform) that have been widely investigated in previous studies (such as in References [23,33,34]), less attention has been paid to the intraplatform basin [20]. Moreover, there exist different points of view on the bottom water redox conditions and OM accumulation mechanisms in the western part of the intraplatform basin [20,39–41]. Previous studies, based on the absence of Ni-Mo sulfide deposits in shale cores and sedimentary iron speciation analysis, suggest that Qiongzhusi Formation shale in the western part of the basin was deposited in an anoxic environment without euxinic bottom waters [39,40] (Figure 1a). Conversely, some studies (such as in References [41,42]) indicate the presence of euxinic bottom waters in the western part of the intraplatform basin (Figure 1a). Consequently, the primary controlling factors for OM enrichment in the lowermost high-total organic carbon (TOC) zone and the mechanism of OM enrichment during the deposition of Qiongzhusi Formation in the western part of intraplatform basin remain unclear.

In this study, we conducted a comprehensive geochemical analysis of the continuous well W207 located in the western part of the intraplatform basin of the Yangtze Platform, South China. This analysis included major elements, trace elements, TOC contents, and Mo isotopes, aiming to reconstruct the bottom water redox conditions and primary productivity conditions during the deposition of lower Cambrian Qiongzhusi Formation shale in the western part of the intraplatform basin, as well as to clarify the primary controlling factors and enrichment mechanisms of OM accumulation at different units.

## 2. Geological Setting

Around 850–820 Ma [23,43,44], the South China Block gradually separated into the Yangtze Block and the Cathaysia Block under intense rifting processes (Figure 1b). During the E-C transition, the Yangtze Block, evolving from a rift basin into a passive continental margin basin, formed a carbonate platform dominated by carbonate deposits, a narrow marginal transitional zone dominated by black chert and shale series (outer shelf), and a deep-water slope and basinal zone dominated by Liuchapo Formation siliceous rocks [9,20,24,45,46] (Figure 1a), with increasing water depth across the three facies belts.

Recent studies have discovered the presence of an intraplatform basin within the carbonate platform, which developed from the Late Ediacaran to Early Cambrian [47,48] (Figure 1a), with the slopes on both sides of the intraplatform basin showing a steeper gradient in the east and a gentler gradient in the west. The distribution of black shales formed during transgressions may be controlled by the intraplatform basin [20,40,48–50]. A newly drilled evaluation well (W207) near the western side of the intraplatform basin provides an opportunity for this study. In the lower Cambrian, the Maidiping Formation, Qiongzhusi Formation, and Canglangpu Formation developed from bottom to top. However, with the uplift and erosion of Tongwan Movement, the Maidiping Formation only exists in some areas in the middle of Yangtze Platform [51,52] and is missing in the W207 well. The Qiongzhusi Formation unconformably overlies the dolomite of the Dengying Formation (Figure 1c).

Stratigraphic correlation of the Qiongzhusi Formation has been carried out through typical marker beds, biostratigraphy, U-Pb ages, cyclostratigraphy, and geochemistry [36,53]. The black shale at the base of the Shiyantou Formation in the Xiaotan section represents the onset of the last appearance of a small shell fossil assemblage (SSFA-3), which can serve as the boundary between the Maidiping and Qiongzhusi Formation [36]. The CA-ID-TIMS zircon U-Pb ages of 526.86 $\pm$ 0.16 Ma in the Meishucun section reported by Yang [54] provide support for the age of the base of the Qiongzhusi Formation. Lower Cambrian Ni-Mo ore layers discovered at the bottom of the GK1 and Z4 wells can be used as a boundary between the second and third stages of the Cambrian, with a Re—Os isochron age of 521 $\pm$ 5 Ma identified within the layers [53].

Based on biostratigraphic division, Liang et al. [55] found that the appearance of *Tsunyidiscus niutitangensis* in the W207 well corresponds to the extreme values of the GR curve at the boundary of Units 3 and 4. This biozone of trilobite may be associated with *Tsunyidiscus acutus-Tsunyidiscus yanjiazhaiensis* at the GR extreme values (3295.89 m) in the JY1 well, and the age of this interval in the JY1 well has been defined at approximately 519.43 Ma [36,56]. Additionally, existing research has shown that the *Tsunyidiscus acutus-Tsunyidiscus yanjiazhaiensis* found at 3295.89 m in the JY1 well can be fully matched with the fossil assemblage of *Tsunyidiscus niutitangensis* that appears in the Jinsha section, possibly representing the first appearance of trilobites [36,56]. The boundary between the Qiongzhusi and Canglangpu Formation in the Xiaotan section is determined as 515 Ma [31], which may reveal the boundary between the Qiongzhusi and Canglangpu Formation in wells such as ZY1 and GK1 [20].

The Qiongzhusi Formation can be divided into four third-order sequences (SQ1, SQ2, SQ3, SQ4) from bottom to top [20,36,57,58]. Combining the previously defined sequence boundaries with the geochemical data in this study, the Qiongzhusi Formation is divided into four units: Unit 1 (3245–3203 m) primarily consists of black shales; Unit 2 (3203–3111 m) mainly comprises interbedded black shales and dark gray siltstone; Unit 3 (3111–3045 m) is primarily composed of lower black shales and upper dark gray siltstone; and Unit 4 (3045–3000 m) mainly consists of black shales with a top layer of dark gray siltstone (Figure 1c).

## 3. Samples and Methods

According to the lithology and thickness of the target interval, uniform sampling was carried out for the Qiongzhusi Formation in the W207 well. A total of 90 samples were measured for TOC analysis, major and trace element analysis, and 30 samples for Mo isotope analysis. The location and depth of sample collection are shown in Figure 1 and Table S1. Of course, before all geochemical analysis, samples with veins, nodules, and phosphatic were removed to ensure the authenticity of the data. Then, the remaining samples were ground to 200 mesh size through hand grinding with agate mortar.

### *3.1. TOC*

First, the carbonate in the powder samples (200 mesh size) was removed through adding hydrochloric acid (10%). Then, the residual hydrochloric acid in the sample was removed through washing with distilled water. After the samples were dried overnight, they were analyzed using the CHNOS Elemental Analyzer (Vario EL III) in the Key Laboratory of Geological Processes and Mineral Resources, China University of Geosciences (Wuhan).

### *3.2. Major and Trace Elements*

The analysis of major elements in the samples was performed using the wavelength-dispersive X-ray fluorescence (XRF) spectrometer AXIOSmAX. Mix the processed powder sample, flux ($Li_2B_4O_7$, $LiBO_2$, LiF) and oxidant ($NH_3NO_3$) in a ratio of 1:10:3. After being heated in a furnace at 1150 °C for 14 min, glass slices were prepared for the XRF test.

Trace elements were analyzed using an Agilent 7700 inductively coupled plasma mass spectrometer (ICP-MS). The volatiles in the samples were removed via burning them in a muffle furnace at 600 °C for 12 h. Then, at a temperature of 190 °C, hydrofluoric acid (HF) and nitric acid ($HNO_3$) were added into the Teflon beaker containing the powder sample for dissolution treatment. The final solution was then analyzed via ICP-MS with a final analysis accuracy better than ±5%.

The enrichment factors can be calculated as follows:

$$X_{EF} = [(X/Al)_{sample}/(X/Al)_{PAAS}], \quad (1)$$

where the "X" is the selected target trace element. The subscript "sample" refers to the weight ratio of element X to AL in this study sample [59], and "PAAS" denotes the Post-Archean Australian Shale (PAAS) standard [60].

### 3.3. Mo Isotopic Compositions ($\delta^{98/95}$Mo)

Mo isotopic compositions were analyzed via Thermo-Fisher Scientific Neptune Plus (MC-ICP-MS) in the State Key Laboratory of Isotope Geochemistry, Guangzhou Institute of Geochemistry, Chinese Academy of Sciences, Guangzhou, China. According to the double-spike method [61], an appropriate amount of $^{97}$Mo–$^{100}$Mo double spikes was added to the sample according to the Mo concentration of the samples. Then, at 130 °C, the sample was dissolved and purified with $HNO_3$, HF, and HCI, and then column separation was performed. The purified Mo was determined via MC–ICP–MS by means of ion-exchange chromatography using BPHA resin [61]. The double-spike and normalizing standard (NIST SRM 3134) was corrected through following the procedure of Siebert et al. [62] and Zhao et al. [63]. At the same time, during the analysis process, the $\delta^{98/95}$Mo of NIST SRM 3134 standard solution and IAPSO seawater was repeatedly measured. The measured values of $\delta^{98/95}$Mo of the two are 0.00 ± 0.05‰ (2SD, n = 15) and 2.06 ± 0.06‰, respectively, which are consistent with the certified values and literature reports [63–65]. Meanwhile, the Mo procedural blank value (<0.1 ng) is much smaller than the total amount of Mo in the samples. Finally, in order to facilitate international comparison and analysis, the $\delta^{98/95}$Mo values in the samples were recalculated based on the NIST SRM 3134 standard solution (0.25‰).

## 4. Results

As shown in Figures 2 and 3 and Table 1, Unit 1 (3245–3203 m) exhibits relatively high TOC contents (average of 2.5 wt.%), ranging from 0.7 to 4.6 wt.%, with a decreasing trend from bottom to top. The $\delta^{98/95}$Mo values vary between −0.25‰ and 2.23‰, displaying a significant fluctuation range. The ratios of U/Th (0.6–4.4) and Ni/Co (2.6–11.3) (Figure 2), as well as the enrichment levels of EF(U) (3.2–22) and EF(Mo) (9.5–204.2), show relatively high values and exhibit similar variations (Figure 3). Additionally, Ni/Al ($6.0 \times 10^{-4}$ to $28.0 \times 10^{-4}$) and Cu/Al ($4.1 \times 10^{-4}$ to $10.0 \times 10^{-4}$) ratios are also relatively high (Figure 2).

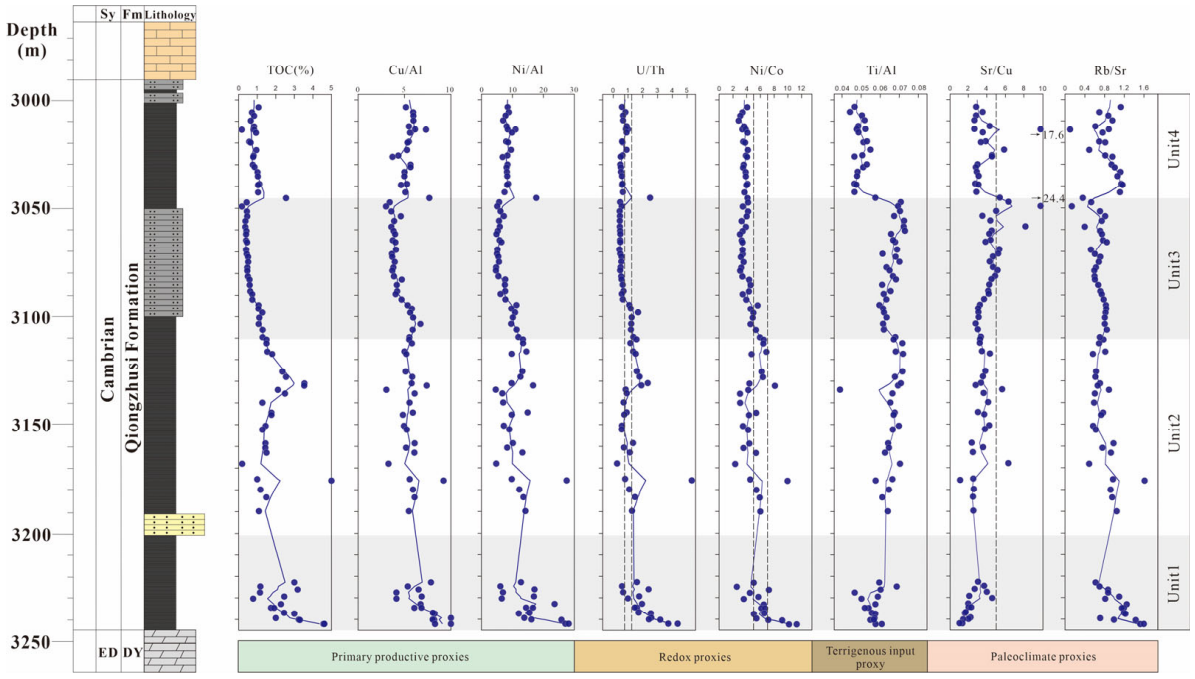


**Figure 2.** Vertical variations of total organic carbon (TOC) contents, primary productivity proxies (Cu/Al, Ni /Al), redox proxies (U/Th, Ni/Co), and terrigenous input proxy (Ti/Al).

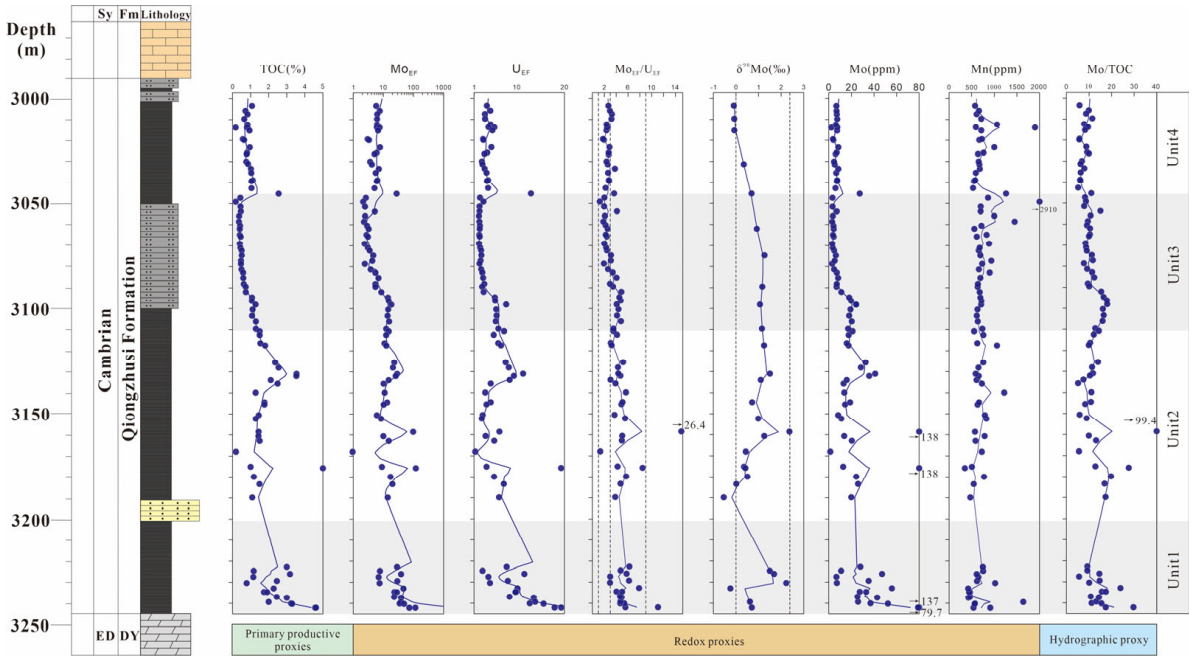


**Figure 3.** Vertical variations of redox proxies (Mo-EF, U-EF, Mo-EF/U-EF, $\delta^{98/95}$Mo, Mo, and Mn) and hydrographic proxy (Mo/TOC).

**Table 1.** Mo isotope ($\delta^{98/95}$Mo) values of the lower Cambrian Qiongzhusi Formation.

| Samples | Member | Depth | $\delta^{98/95}$Mo | $\delta^{98/95}$Mo(auth) [1] | 2SE [2] |
|---|---|---|---|---|---|
| | | m | ‰ | ‰ | |
| W207-90 | Unit 4 | 3003.41 | −0.10 | −0.17 | 0.04 |
| W207-87 | Unit 4 | 3009.68 | −0.08 | −0.14 | 0.03 |
| W207-83 | Unit 4 | 3015.33 | −0.07 | −0.13 | 0.03 |
| W207-76 | Unit 4 | 3031.33 | 0.35 | 0.33 | 0.02 |
| W207-70 | Unit 4 | 3045.35 | 0.69 | 0.70 | 0.03 |
| W207-62 | Unit 3 | 3061.96 | 0.92 | 1.02 | 0.03 |
| W207-56 | Unit 3 | 3074.73 | 1.26 | 1.37 | 0.03 |
| W207-52 | Unit 3 | 3082.83 | 1.21 | 1.29 | 0.03 |
| W207-49 | Unit 3 | 3089.48 | 1.17 | 1.25 | 0.03 |
| W207-45 | Unit 3 | 3098.12 | 1.06 | 1.08 | 0.04 |
| W207-41 | Unit 3 | 3109.60 | 1.15 | 1.18 | 0.02 |
| W207-37 | Unit 2 | 3117.42 | 1.24 | 1.28 | 0.03 |
| W207-34 | Unit 2 | 3131.03 | 1.50 | 1.52 | 0.03 |
| W207-32 | Unit 2 | 3134.00 | 1.10 | 1.14 | 0.04 |
| W207-29 | Unit 2 | 3144.47 | 0.72 | 0.73 | 0.03 |
| W207-26 | Unit 2 | 3152.30 | 0.99 | 1.03 | 0.02 |
| W207-25 | Unit 2 | 3158.59 | 2.37 | 2.38 | 0.03 |
| W207-24 | Unit 2 | 3160.66 | 1.25 | 1.30 | 0.02 |
| W207-22 | Unit 2 | 3168.00 | 0.43 | 0.47 | 0.03 |
| W207-21 | Unit 2 | 3175.10 | 0.36 | 0.35 | 0.02 |
| W207-20 | Unit 2 | 3175.74 | 0.42 | 0.42 | 0.02 |
| W207-19 | Unit 2 | 3179.90 | 0.51 | 0.51 | 0.03 |
| W207-18 | Unit 2 | 3183.42 | 0.01 | 0.00 | 0.02 |
| W207-17 | Unit 2 | 3189.80 | −0.54 | −0.58 | 0.04 |
| W207-15 | Unit 1 | 3224.68 | 1.50 | 1.58 | 0.03 |
| W207-14 | Unit 1 | 3226.13 | 1.69 | 1.71 | 0.03 |
| W207-11 | Unit 1 | 3230.37 | 2.23 | 2.41 | 0.03 |
| W207-10 | Unit 1 | 3232.92 | −0.25 | −0.25 | 0.03 |
| W207-05 | Unit 1 | 3239.40 | 0.62 | 0.62 | 0.03 |
| W207-02 | Unit 1 | 3242.10 | 0.70 | 0.70 | 0.03 |

[1] The corrected $\delta^{98/95}$Mo values were calculated following the formula: $\delta^{98/95}Mo_{auth} = [(\delta^{98/95}Mo_{tot} \times Mo_{tot} - \delta^{98/95}Mo_{det} \times Mo_{det})/Mo_{auth}]$ [66–68], in which the detrital Mo concentration ($Mo_{det}$) was given by $Mo_{det} = [(Mo/Al)_{PAAS} \times Al_{tot}]$ and the authigenic Mo concentration was calculated by $Mo_{auth} = Mo_{tot} - Mo_{det}$. Mo and Al concentration of PAAS (1.0 ppm, 10%, respectively) [60] and $\delta^{98/95}Mo_{det}$ value of 0.4‰ [69] were used for detritus correction. [2] 2SE means double of Standard Error.

In Unit 2 (3203–3111 m), the TOC content varies from 0.2 to 5.0 wt.%, with an average of 1.9 wt.%. The $\delta^{98/95}$Mo values range from −0.54‰ to 2.37‰, gradually increasing from the bottom to the middle part of the unit (3158.59 m), and then decreasing. The ratios of U/Th (0.3–5.3) and Ni/Co (2.3–10.0) (Figure 2), as well as the enrichment levels of EF(U) (1.5–23.7) and EF(Mo) (1.9–200.1), show relatively consistent values compared to Unit 1 (Figure 3). The ratios of Ni/Al ($4.5 \times 10^{-4}$ to $27.4 \times 10^{-4}$) and Cu/Al ($3.0 \times 10^{-4}$ to $9.2 \times 10^{-4}$) exhibit similar trends (Figure 2), with higher values at the bottom and lower values in the middle part of Unit 2.

In Unit 3 (3111–3045 m), the TOC content ranges from 0.2 to 1.5 wt.%, with an average of 0.7 wt.%, relatively lower compared to Unit 1 and Unit 2. It gradually decreases in the vertical direction. The $\delta^{98/95}$Mo values are relatively stable, fluctuating between 0.92‰ and 1.26‰, with a decreasing trend in the vertical direction (Figure 3). The ratios of U/Th (0.4–1.7) and Ni/Co (3.0–6.5), as well as the enrichment levels of EF(U) (2.4–8.3) and EF(Mo) (4.3–33.2), are relatively low and show small variations. The ratios of Ni/Al ($4.6 \times 10^{-4}$–$13.3 \times 10^{-4}$) and Cu/Al ($3.0 \times 10^{-4}$–$6.7 \times 10^{-4}$) gradually decreased from the bottom and then rebounded at the top of the interval, lower than those of Unit 1 and Unit 2 (Figure 2).

In Unit 4 (3045–3000 m), the TOC content varies between 0.2 and 2.5 wt.% (average of 0.9 wt.%), obviously higher than that of Unit 3. The $\delta^{98/95}$Mo values continued to decrease from 0.69‰ to −0.10‰ (Figure 3). The enrichment degree of U/Th (0.5–2.5) and Ni/Co (2.8–4.1) ratios, as well as EF(U) (2.4–12.6) and EF(Mo) (4.6–46.0), was relatively low within this interval. The Ni/Al ($6.8 \times 10^{-4}$–$17.6 \times 10^{-4}$) and Cu/Al ($3.7 \times 10^{-4}$–$7.7 \times 10^{-4}$) ratios showed a noticeable increase compared to the third stage, steadily rising upwards (Figure 2).

## 5. Discussion

### 5.1. The Degree of Oxygenation in the Bottom Water Environment Continues to Increase

The ratios of U/Th and Ni/Co have been widely used to reconstruct paleoceanic redox environments [17,70–74]. The U/Th and Ni/Co ratios in Unit 1 (average of 2.10 and 6.41, respectively) and Unit 2 (average of 1.32 and 5.13, respectively) were relatively high, reflecting an anoxic environment. The relatively low values of these ratios in Unit 3 (average of 0.73 and 4.06) and Unit 4 (average of 0.77 and 3.71) reflect a relatively stable oxic–suboxic environment (Figure 2). Relatively low U/Th and Ni/Co ratios suggest an upward enhancement in the oxidation state of the bottom water environment on the western side of the intraplatform basin [68,73,75,76] (Figure 2). This interpretation is consistent with redox conditions inferred from Mo content, EF(Mo)/EF(U), and Mo/TOC ratios (Figures 3 and 4a).

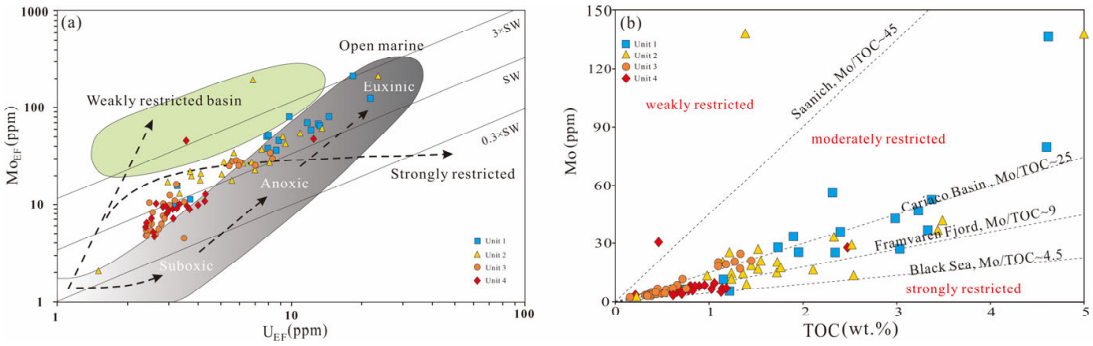


**Figure 4.** (**a**) EF(Mo) versus EF(U) for Qiongzhusi Formation samples [77,78]. The solid line represents the Mo: U ratio in modern seawater. (**b**) Sediment Mo versus TOC for the Qiongzhusi Formation samples. Four representatives of the modern anoxic basin system (Saanich Inlet, Cariaco Basin, Framvaren Fjord, and Black Sea) are represented by dashed lines in the figure, which reflect different degrees of hydrographic restriction [79].

It should be noted that in restricted environments, Mo concentrations in the water column may decrease due to the lack of open ocean inputs [80–82]. In Unit 1, the Mo content (average of 40.67) and EF(Mo)/EF(U) ratios (5.42 on average) support the anoxic environment indicated by the U/Th and Ni/Co ratios. The extreme point observed in sample W-02 (3242.1 m) (Mo content of 137 ppm, EF(Mo)/EF(U) ratios of 11.06) reflects a possible weakly euxinic environment in the water column (Figure 3). Combining the sea level change curve [36] and various trace elements such as EF(Mo) and EF(U) (Figures 1c and 3), Unit 2 can be divided into two cycles that first increase and then decrease. The relative high points of these cycles (W-20 at 3131 m and W-34 at 3175.7 m) correspond to the occurrence of two transgressive events. The large-scale transgressions connected the intraplatform basin to the open sea, replenishing trace elements (Mo, U, etc.) and increasing the degree of water reduction. A weakly euxinic condition may have occurred at 3175 m (Figure 3), which is consistent with no significant correlation between the TOC and redox-sensitive trace elements such as U/Th, Ni/Al and Cu/Al in this point [83] (Figure 5a–f). Considering the anoxic environment indicated by the U/Th and Ni/Co ratios in Unit 2, the EF(Mo)/EF(U) ratios (average of 5.45) likely indicate dominant anoxic with occasional and weakly euxinic water conditions. This viewpoint is supported by Mo isotope evidence (see details in Section 5.2). Similar short-term euxinic events in anoxic environments have also been observed in the ZY1 well and Jinsha section on the eastern side of the intraplatform basin during the same time [20,31]. In Units 3 and 4, the occurrence of the regression event during Cambrian Age 3 was accompanied by the development of oxidizing bottom water conditions. This interpretation is consistent with the low EF(Mo)/EF(U) ratios (average of 3.09, 3.14) representing an oxic–suboxic environment. From bottom to top, the Qiongzhusi Formation experienced an anoxic–euxinic–oxic–suboxic bottom water environment.

The redox environment of bottom water is closely related to the hydrographic conditions of the basin. The Mo/TOC ratio has been widely used as an indicator of basin water connectivity limitations [81] (Figure 4b). However, due to the possibility of lower Mo concentrations in early Cambrian oceans compared to modern seawater [84–86], Cheng et al. [87] suggested that when the Mo/TOC ratio in sediments exceeds 11 ppm/wt.%, good connectivity between the basin and the open sea can be considered. In Unit 1, the relatively high Mo/TOC values (average of 14.52 ppm/wt.%) indicate low basin water restrictiveness, favorable for the existence of anoxic bottom water environments. The Mo/TOC values in Unit 2 correspond well to the two transgression events, indicating increasing basin openness with the occurrence of transgressions. The oxic–suboxic environment in Unit 3 corresponds to the regression during Cambrian Age 3 (Figures 1c and 3), and the weakening connection between the basin and the open sea prevents the replenishment of Mo consumed in the ocean, resulting in a decrease in Mo and U values (average of 8.78 and 7.86, respectively) [81]. In Unit 4, the level of basin restrictiveness further increased, accompanied by a decrease in Mo/TOC values (Figure 4b).

### 5.2. $\delta^{98/95}$Mo Isotopes and Related Redox Conditions

Mo isotopes in organic-rich sedimentary rocks have been widely used in reconstructing local and global marine redox states because it exhibits high sensitivity to redox conditions [65,67,75,86,88–91]. There are two main modes of Mo output in the ocean. In oxic environments, iron or manganese oxides preferentially adsorb the light Mo isotope, resulting in significant isotope fractionation between sediments and seawater, up to ~3% fractionation [92,93]. In euxinic environments, when the concentration of $H_2S$ in the water solution is high ($[H_2S]aq > 11$ μM), oxyanion molybdate ($MoO_4^{2-}$), as the main form of modern seawater Mo, is almost completely converted to oxythiomolybdate species ($MoO_{4-x}S_x^{2-}$, x = 1–4), with little isotope fractionation [66,94]. When the concentration of $H_2S$ in the water solution is low ($[H_2S]aq < 11$ μM), the incomplete conversion of molybdate ($MoO_4^{2-}$) leads to significant isotope fractionation in the sedimentary Mo isotopes [92,95]. This also explains why Mo isotopes can serve as redox proxies. Before analyzing the

Mo isotopes, we eliminated possible detrital effects using the method proposed by Wen et al. [67]. The corrected results show that the measured Mo isotope values ($\delta^{98/95}$Mo) are nearly equivalent to the corrected values ($\delta^{98/95}Mo_{auth}$) (Table 1), indicating a minimal impact of detrital Mo on bulk Mo isotopes. Therefore, we directly discuss the measured values in the following discussion.

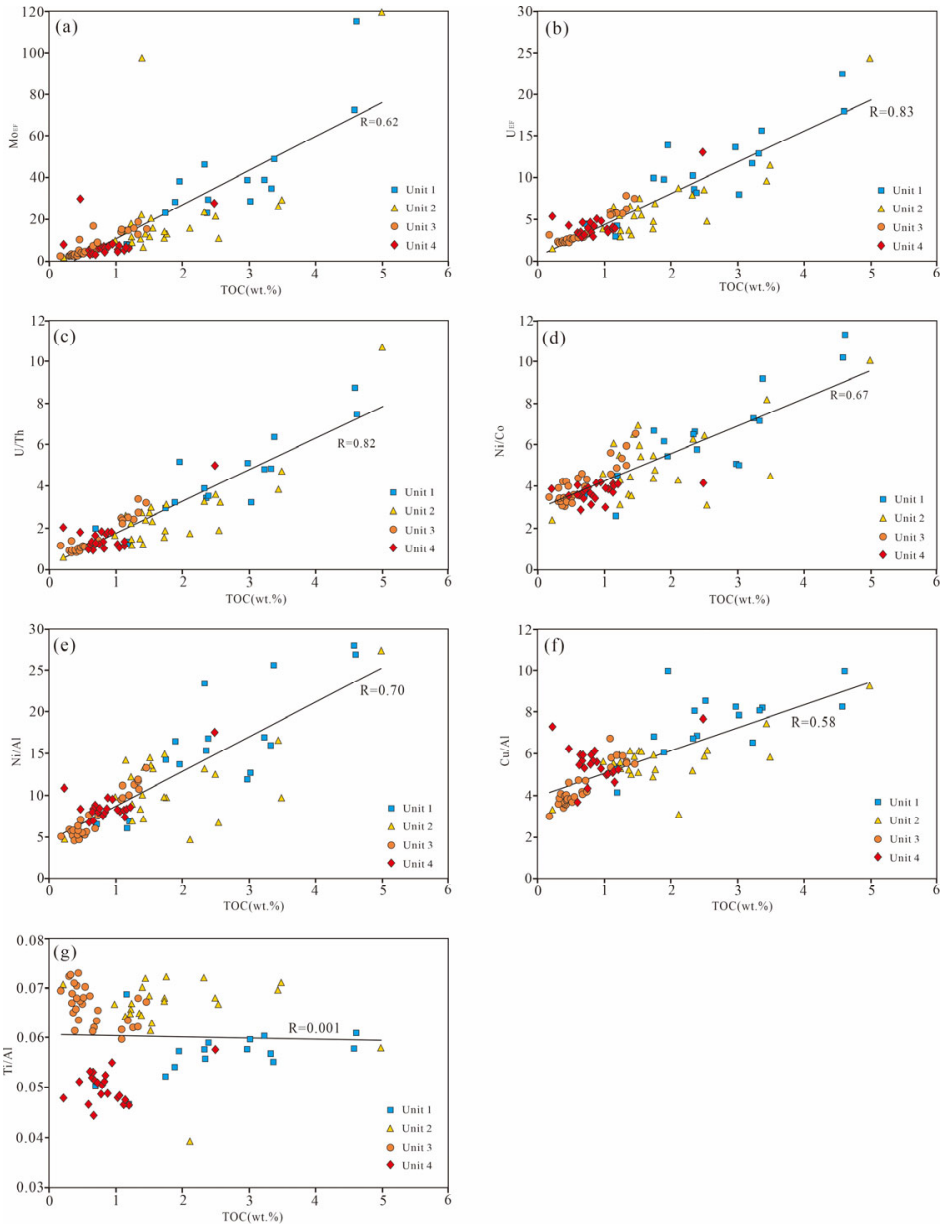


**Figure 5.** Relationships between TOC contents and (**a**) Mo-EF; (**b**) U-EF; (**c**) U/Th ratios; (**d**) Ni/Co ratios; (**e**) Ni/Al; (**f**) Cu/Al ratios; (**g**) Ti/Al ratios of Qiongzhusi Formation samples.

The presence of weak euxinia in the anoxic bottom water conditions has been confirmed by $\delta^{98/95}$Mo values from the western core of the intraplatform basin. Negative $\delta^{98/95}$Mo values (−0.08‰ to −0.54‰) appear at the bottom of Units 1 and 2 (Figure 3). The occurrence of negative Mo isotopes can usually be attributed to three possible mechanisms: the first possibility is Fe-$Mn_{ox}$ adsorption in the oxic environment [96], but the higher U/Th and Ni/Co ratios in Unit 1 and 2 preclude this possibility. The second possibility is Fe-$Mn_{ox}$ shuttling [68,87,97,98], similar to the modern Baltic Sea and Cariaco Basin [97,99]. Under the shuttle effect of iron and manganese oxide, lighter Mo isotopes enter the sediment,

leading to negative $\delta^{98/95}$Mo values. In this case, euxinic conditions in the sediment result in preferential enrichment of Mo relative to U, producing higher EF(Mo)/EF(U) ratios (~3 × SW) and relatively higher Mo concentrations. At the same time, the lack of support for reductive dissolution inhibits Mn accumulation in the sediment, resulting in a relative deficiency of Mn. The EF(Mo)/EF(U) ratios (7.86) and Mo (55.8 ppm) and Mn (424 ppm) values in sample W-10 at the bottom of Unit 2 support the possibility of Fe-$Mn_{ox}$ shuttling. It is worth mentioning that samples W-02 and W-34, mentioned in Section 5.1, also support the possibility of Fe-$Mn_{ox}$ shuttling with their negative $\delta^{98/95}$Mo values (0.7‰ and 0.42‰, respectively). The third possibility is based on the incomplete conversion of molybdate ($MoO_4^{2-}$) under weakly euxinic water conditions ([$H_2S$]aq < 11μM), causing Mo isotopic fractionation [94,99]. The EF(Mo)/EF(U) ratios of samples with negative $\delta^{98/95}$Mo values in Unit 2 are only about twice that of modern seawater (~1 × SW), which excludes the possibility of Fe-$Mn_{ox}$ shuttling. Therefore, the negative $\delta^{98/95}$Mo values in Unit 2 may be attributed to significant fractionation caused by the incomplete conversion of molybdate ($MoO_4^{2-}$) under weakly euxinic water conditions. In addition, although Unit 1 is predominantly anoxic, the occurrence of Fe-$Mn_{ox}$ shuttling in samples W-02 and W-10, mentioned above, demonstrates the presence of localized euxinic environments in Unit 1. Thus, the appearance of negative $\delta^{98/95}$Mo values in sample W-02 in Unit 1 may also be due to the incomplete conversion of molybdate ($MoO_4^{2-}$) under weakly euxinic water conditions or the combined effects of both (such as in Reference [68]).

Except for the negative $\delta^{98/95}$Mo values, samples W-11 (2.23‰) and W-25 (2.37‰) in Units 1 and 2 exhibit relatively high $\delta^{98/95}$Mo values. Similar high values have been reported in profiles from the Yangtze Block and Tarim Basin during the same interval [67,86,87]. The $\delta^{98/95}$Mo values reported by Chen et al. [100] (~+2.3‰) may reflect the highest $\delta^{98/95}$Mo values of Early Cambrian oceanic seawater, and the two high values are nearly equivalent to contemporaneous seawater $\delta^{98/95}$Mo values (Figure 3), which may indicate smaller isotope fractionation under high-$H_2S$ conditions. The Mo isotopes exhibit significant fluctuations (−0.54‰ to 2.37‰) (Figure 3) in Unit 1 and in the lower part of Unit 2 (before the transgression). Except for samples W-02, W-10, and W-34, mentioned earlier, the other samples did not exhibit Fe-$Mn_{ox}$ shuttling. Such a large range of fluctuations may reflect isotope fractionation under weakly euxinic water conditions [68,95,99]. Overall, whether it is the extreme points that partially appear or the overall fluctuations in Units 1 and 2, these suggest the development of weakly euxinic conditions in the intraplatform basin.

From 3131 m in Unit 2 to 3000 m in Unit 4, Mo isotopes exhibit a decreasing trend, showing a negative bias since the large-scale transgression of Cambrian Stage 2 (Figures 1c and 3). The average $\delta^{98/95}$Mo value of Ni-Mo sulfide ore layers formed during the transgression in the Maluhe and Dazhuliushui profiles is reported as 1.13 ± 0.14‰ (n = 11), which is consistent with the $\delta^{98/95}$Mo values near the location of the Ni-Mo sulfide ore layers in the W207 well (average of 1.18‰, n = 6) [68,101] (Figure 3). Subsequently, with ongoing regression, the confinement of the intraplatform basin gradually increased, possibly leading to a gradual decrease in Mo isotopic values in the intraplatform seawater to values near those of continental input (+0.7‰) [68,101] (Figure 3).

### *5.3. Relatively Low Primary Productivity May Be Associated with the Absence of Upwelling*

Previous studies suggested that primary productivity can be reconstructed through various geochemical indicators, including TOC values, organic biomarkers, C and N isotopes, and other trace elements such as P, Ba, Cu, and Ni [38,102–105]. Cu and Ni elements, which are essential nutrients for the growth of phytoplankton in the photic zone, are often associated with OM in sediments [103]. Considering that the assessment of productivity may not be accurate when relying solely on a single indicator [102,106], we studied variations in primary productivity based on multiple indicators (TOC, Cu, Ni) and eliminated the dilutive effects of detrital fractions on Cu and Ni. Cu/Al and Ni/Al showed a strong correlation with TOC (Figure 5e,f) ($r = 0.58$, $p(\alpha) < 0.05$ for Cu/Al vs.

TOC and r = 0.70, p(α) < 0.05 for Ni/Al vs. TOC), suggesting that most of the Cu and Ni are related to OM and can be used to reconstruct primary productivity in surface waters [20,103]. The shale Cu/Al ratios in the Qiongzhusi Formation minorly decreased from Unit 1 ($4.13 \times 10^{-4}$–$10.0 \times 10^{-4}$, average of $7.20 \times 10^{-4}$) to Unit 3 ($3.0 \times 10^{-4}$–$6.72 \times 10^{-4}$, average of $4.41 \times 10^{-4}$), and then increased in Unit 4 ($3.71 \times 10^{-4}$–$7.67 \times 10^{-4}$, average of $5.53 \times 10^{-4}$), indicating a slight decline in surface water bioproductivity followed by a significant increase upward (Figure 2). A similar trend was also observed in the Ni/Al ratios and TOC values. The Cu/Al ($5.47 \times 10^{-4}$) and Ni/Al ($10.2 \times 10^{-4}$) ratios from well W207 are lower than the corresponding ratios observed in the deep-water slope and basinal facies of well TX-1 (Cu/Al = $31.36 \times 10^{-4}$, Ni/Al = $29.46 \times 10^{-4}$) [34]. This finding is consistent with the conclusions in previous studies [20,107] that the productivity of the intraplatform basin facies is lower than the well-developed upwelling events found in the deep-water slope and basinal facies.

Upwelling events are one of the important factors affecting the accumulation of OM and are widely reported in other facies of the Yangtze Platform [23,31,34] (Figures 6a,b and 7). Nevertheless, within the intraplatform basin, the impact of upwelling on OM accumulation remains unclear. Upwelling from the deep sea is often enriched in cadmium (Cd) elements and relatively depleted in cobalt (Co) and manganese (Mn) elements, so when EF(Co)*EF(Mn) < 0.5 or Co*Mn < 0.4, it is considered to indicate the presence of upwelling. Conversely, when EF(Co)*EF(Mn) > 2 or Co*Mn > 0.4, it indicates a restrictive environment [108] (Figure 6a,c). The EF(Co)*EF(Mn) values (0.36–13.84, average of 1.32) and Co*Mn values (0.64–3.40, average of 1.11) of the Qiongzhusi Formation indicate a relatively restricted environment (Figure 6c,d; Table S2), which is further supported by the relatively low Mo/TOC ratios (Figures 3 and 4b).

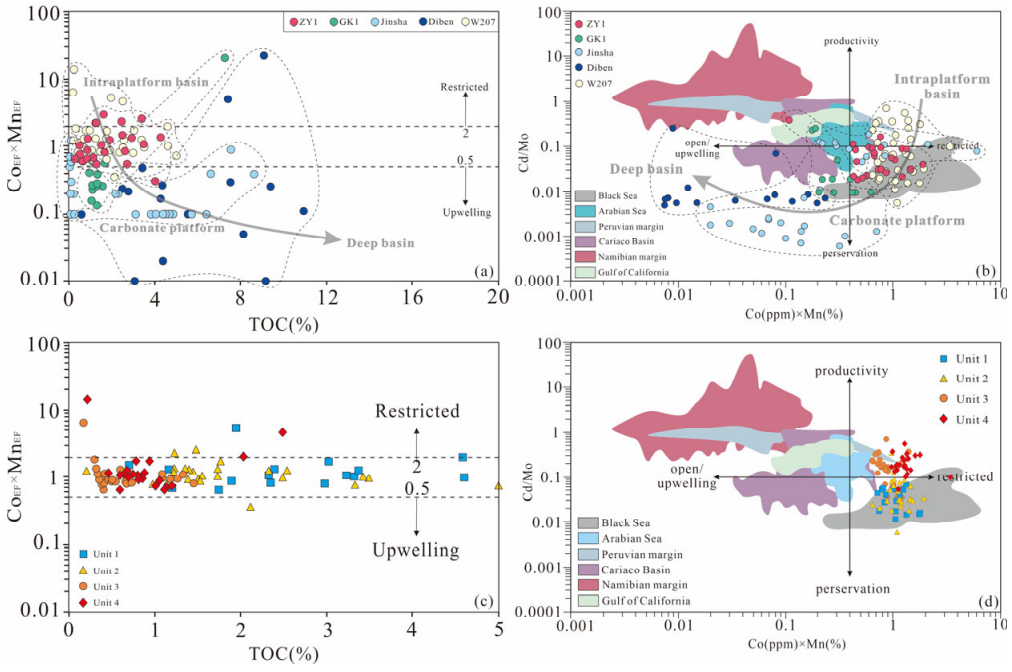


**Figure 6.** Cross-plots of (**a**,**c**) TOC versus Co-EF × Mn-EF, (**b**,**d**) Co (ppm) × Mn (%) versus Cd/Mo ratios of the Qiongzhusi Formation and its equivalents samples [108]. The sample data in (**a**,**b**) come from published data of different sections and wells in the Yangtze Block. Data sources: ZY1 [20]; GK1 [46]; Jinsha [31]; Diben [20]; W207 (this study, only part of the sample is shown). c and d show the samples of four different units of the Qiongzhusi Formation in Well W207 (this study).

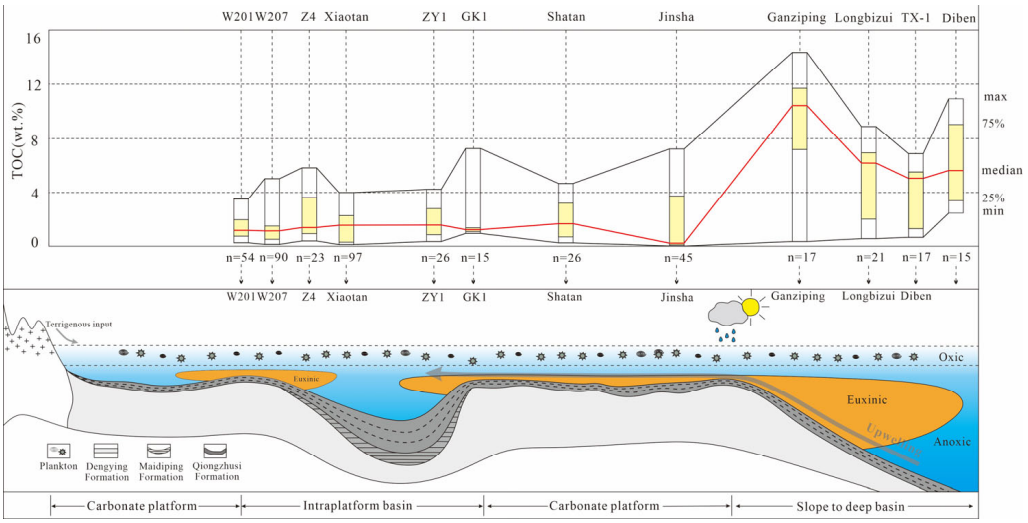


**Figure 7.** Simplified model of organic matter accumulation control during shale deposition of Qiongzhusi Formation in different facies belts of Yangtze block. TOC data of sections and wells are from Wang et al. [40], Wang et al. [42], Cremonese et al. [109], Gao et al. [20,46], Jin et al. [31,39], Chen et al. [24], Wang et al. [9], Yuan et al. [110].

In the Yangtze Platform, multiple profiles of EF(Co)*EF(Mn) and Co*Mn values within various sedimentary facies reveal a progressive increase in upwelling events from the intraplatform basin towards the deep-water slope and basinal facies. This trend is accompanied by a gradual rise in TOC values (Figures 6a,b and 7). Early findings suggested that upwelling, prevalent within deep-water slope and basinal facies, carried nutrients that effectively enhanced the primary productivity of surface waters, serving as a primary factor for OM accumulation in these regions [23,31,32,34,111]. The EF(Co)*EF(Mn) and Co*Mn values from multiple profiles also corroborate this observation (Figure 6a,b). Therefore, the relatively lower primary productivity in the intraplatform basin facies could potentially be attributed to the absence of upwelling events (Figure 6c,d, and Figure 7). This is in contrast to the deep-water slope and basinal facies, which are characterized by significant upwelling occurrences.

### *5.4. Mechanisms of OM Enrichment*

The enrichment of OM is often influenced by various events, such as sea level changes, upwelling events, and terrigenous input [32,72,86,111–115]. The impact of these events on OM enrichment varies in different geological settings but is ultimately manifested through the control of primary productivity and bottom water preservation conditions [29,72,116].

During the deposition of Unit 1 in Cambrian Stage 2, the strong correlation between redox indices such as U/Th and TOC ($R = 0.82$, $p(\alpha) < 0.05$) suggests that the main bottom water conditions are anoxic, providing favorable conditions for the preservation of OM. The relatively high sea level allowed the intraplatform basin to be connected to the open sea, and the input of nutrients sustained high primary productivity. This is consistent with the correlation exhibited by Cu/Al ($R = 0.52$, $p(\alpha) < 0.05$), Ni/Al ($R = 0.67$, $p(\alpha) < 0.05$), and TOC (Figure 5e,f). Thus, the development of anoxic and high productivity is favorable for increased OM accumulation and preservation (Figure 8A).

Relative sea level changes in the intraplatform basin controlled the redox conditions during the deposition of Unit 2 [117]. Intermittent euxinic and continuous anoxic environments account for the relatively high TOC values. Relatively high primary productivity continuously contributed to OM enrichment with the absence of upwelling events.

During the deposition of Unit 3, as the sea level gradually falls in Cambrian Stage 3, the increasing restriction within the basin led to a reduction in nutrient supply and a decline in primary productivity. At the same time, the predominant bottom water conditions changed

from anoxic to suboxic, leading to poor preservation conditions for OM. In addition, the weak negative correlation between Ti/Al and TOC ($R = -0.28$, $p(\alpha) > 0.05$) indicated the dilution effect of increasing terrigenous input on OM [115] (Figure 5g). Thus, the low OM content in Unit 3 should be attributed to low productivity, relatively oxidizing conditions, and the dilution of terrigenous input (Figure 8B).

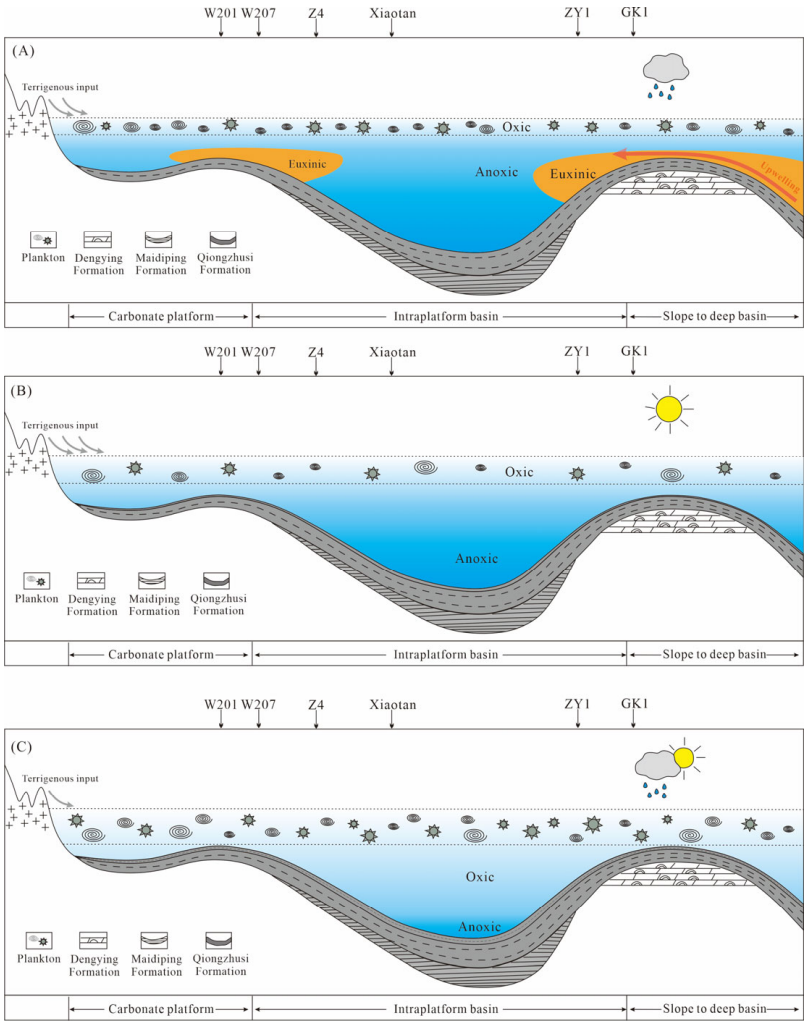


**Figure 8.** Organic matter accumulation models of Qiongzhusi Formation. (**A**) Units 1 and 2, anoxic bottom water conditions and high primary productivity. (**B**) Unit 3, suboxic bottom water conditions, low primary productivity, and high terrigenous input. (**C**) Unit 4, oxic–suboxic bottom water conditions, relatively high primary productivity, warm and humid climate, and low terrigenous input. Data sources: W201 [40]; W207 (this study); Z4 [42]; Xiaotan [39]; ZY1 [20]; GK1 [46].

Although Unit 4 is still in an oxidizing environment, its TOC value (0.2–2.5 wt.%, average of 0.9 wt.%) showed a recovery compared to Unit 3. A rapid decrease in Ti/Al ratios indicated a weakening of terrigenous input, which may reflect a transition from arid to humid climate in the intraplatform basin [18,23,118,119] (Figure 2). This change is also consistent with the increase in Rb/Sr ratios and decrease in Sr/Cu ratios (Table S2; Figure 2). The relatively warm and humid climate in Unit 4 promoted the bloom of surface water organisms, which is consistent with the first appearance of *Tsunyidiscus niutitangensis* in the lower part of Unit 4 [55], indicating relatively higher primary productivity. Overall, although the widespread oxic–suboxic bottom water conditions in the intraplatform basin are unfavorable for the preservation of OM, the increase in primary productivity and the weakening of terrigenous clastic input have relatively compensated for this deficiency (Figure 8C).

Sweere's analysis of multiple global regions indicates (Figure 6b,d) that Cd/Mo > 0.1 and Co*Mn < 0.4 represent upwelling environments driven by productivity (e.g., Namibian margin, Peruvian margin), while Cd/Mo ratios < 0.1 and Co*Mn > 0.4 reflect restricted basin settings driven by preservation conditions (e.g., the Black Sea). From the Cd/Mo ratios of the four units in this study (Figure 6d), it can be seen that Unit 1 and Unit 2 sample points are mainly located in the "preservation" area, while Unit 3 and Unit 4 samples are mainly located in the "productivity" area.

This is consistent with the TOC values of the shales in Units 1 and 2 being much higher than those in Units 3 and 4. This indicates that preservation conditions are more crucial than productivity conditions in restricted environments that lack upwelling and that they play a critical role in the development of high-quality hydrocarbon source rocks. The enrichment mechanism in the intraplatform basin significantly differs from other facies in the Yangtze Platform, such as the deep-water slope and basinal facies, primarily driven by productivity, or the transitional facies, influenced by both productivity and preservation conditions [20,34,107].

## 6. Conclusions

(1) During the deposition of the Cambrian Qiongzhusi Formation, the western side of the intraplatform basin within the Yangtze Platform experienced a transition from continuous anoxic conditions with intermittent euxinic to oxic–suboxic bottom water environments. The highly redox-sensitive $\delta^{98/95}$Mo values in Units 1 and 2 support the presence of weakly euxinic conditions in the early Cambrian period, further elucidating the redox environment of the bottom water during this interval.

(2) EF(Co) * EF(Mn) values suggest an absence of upwelling within the intraplatform basin, which diverges from other regions within the Yangtze Platform that showcase substantial upwelling events. The relatively lower primary productivity in the intraplatform basin facies could potentially be attributed to the lack of upwelling events. Primary productivity exhibited a trend of gradual decline from stages 1 to 3, followed by an increase in stage 4.

(3) Qiongzhusi Formation shale exhibits variations in the mechanisms for OM enrichment across distinct units. The lower portion of the Qiongzhusi Formation on the western side of the intraplatform basin (Units 1 and 2) is predominantly influenced by preservation conditions, while the upper portion (Units 3 and 4) is primarily affected by productivity conditions. This indicates that in constrained environments devoid of upwelling, preservation conditions assume a more pivotal role in OM enrichment. This discovery offers valuable insights for the exploration of high-quality hydrocarbon source rocks within the intraplatform basin.

**Supplementary Materials:** The following supporting information can be downloaded at: https://www.mdpi.com/article/10.3390/jmse11101907/s1, Table S1: Total organic carbon (TOC) and Major elements compositions of the lower Cambrian Qiongzhusi Formation; Table S2: Selected trace elements concentrations and enrichment factors of the lower Cambrian Qiongzhusi Formation.

**Author Contributions:** Conceptualization, E.L. and Q.Z.; methodology, Q.Z.; software, R.Z.; validation, E.L., S.P. and Z.Z.; formal analysis, E.L.; investigation, Q.Z.; resources, S.P.; data curation, Z.J.; writing—original draft preparation, Q.Z.; writing—review and editing, E.L.; visualization, Q.Z.; supervision, H.W.; project administration, S.P.; funding acquisition, H.W. All authors have read and agreed to the published version of the manuscript.

**Funding:** This research was funded by Science and Technology Research Project for the Research Institute of Petroleum Exploration and Development, China National Petroleum Corporation (2021YJCQ03).

**Institutional Review Board Statement:** Not applicable.

**Informed Consent Statement:** Not applicable.

**Data Availability Statement:** The data presented in this study are available on request from the corresponding author.

**Acknowledgments:** We appreciate Research Institute of Petroleum Exploration and Development for providing the data and permission to publish this paper. We are also very grateful to the reviewers and editors for their contributions to improving this paper.

**Conflicts of Interest:** The authors declare no conflict of interest.

## References

1. Knoll, A.H.; Carroll, S.B. Early animal evolution: Emerging views from comparative biology and geology. *Science* **1999**, *284*, 2129–2137. [CrossRef]
2. Kimura, H.; Watanabe, Y. Oceanic anoxia at the Precambrian-Cambrian boundary. *Geology* **2001**, *29*, 995–998. [CrossRef]
3. Amthor, J.E.; Grotzinger, J.P.; Schroder, S.; Bowring, S.A.; Ramezani, J.; Martin, M.W.; Matter, A. Extinction of Cloudina and Namacalathus at the Precambrian-Cambrian boundary in Oman. *Geology* **2003**, *31*, 431–434. [CrossRef]
4. Marshall, C.R. Explaining the Cambrian "Explosion" of Animals. *Annu. Rev. Earth Planet. Sci.* **2006**, *34*, 355–384. [CrossRef]
5. Jiang, S.Y.; Pi, D.H.; Heubeck, C.; Frimmel, H.; Liu, Y.P.; Deng, H.L.; Ling, H.F.; Yang, J.H. Early Cambrian ocean anoxia in South China. *Nature* **2009**, *459*, E5–E6. [CrossRef]
6. Zhang, F.F.; Xiao, S.H.; Romaniello, S.J.; Hardisty, D.; Li, C.; Melezhik, V.; Pokrovsky, B.; Cheng, M.; Shi, W.; Lenton, T.M. Global marine redox changes drove the rise and fall of the Ediacara biota. *Geobiology* **2019**, *17*, 594–610. [CrossRef]
7. Steiner, M.; Wallis, E.; Erdtmann, B.D.; Zhao, Y.; Yang, R. Submarine-hydrothermal exhalative ore layers in black shales from South China and associated fossils—Insights into a Lower Cambrian facies and bio-evolution. *Palaeogeogr. Palaeoclimatol. Palaeoecol.* **2001**, *169*, 165–191. [CrossRef]
8. Zhu, M.; Strauss, H.; Shields, G.A. From snowball earth to the Cambrian bioradiation: Calibration of Ediacaran-Cambrian earth history in South China. *Palaeogeogr. Palaeoclimatol. Palaeoecol.* **2007**, *254*, 1–6. [CrossRef]
9. Wang, J.G.; Chen, D.Z.; Yan, D.T.; Wei, H.Y.; Xiang, L. Evolution from an anoxic to oxic deep ocean during the Ediacaran-Cambrian transition and implications for bioradiation. *Chem. Geol.* **2012**, *306–307*, 129–138. [CrossRef]
10. Demaison, G.; Moore, G. Anoxic environments and oil source bed genesis. *Org. Geochem.* **1980**, *2*, 9–31. [CrossRef]
11. Tyson, R.V. Deposition of Organic-Carbon-Rich Sediments: Models Mechanisms, and Consequences. In *The "Productivity versus Preservation" Controversy: Cause, Flaws, and Resolution*, 1st ed.; Harris, N.B., Ed.; SEPM Special Publication: Tulsa, OK, USA, 2005; Volume 82, pp. 17–33. ISBN 9781565762183.
12. Murphy, A.E.; Sageman, B.B.; Hollander, D.J.; Lyons, T.W.; Brett, C.E. Black shale deposition and faunal overturn in the Devonian Appalachian Basin; clastic starvation, seasonal water–column mixing, and efficient biolimiting nutrient recycling. *Paleoceanography* **2000**, *15*, 280–291. [CrossRef]
13. Abdi, Z.; Rimmer, S.M.; Rowe, H.D.; Nordeng, S. Controls on organic matter accumulation in the bakken formation, williston basin, USA. *Chem. Geol.* **2021**, *586*, 120588. [CrossRef]
14. Si, L.L.; Wei, J.P.; Xi, Y.J.; Wang, H.Y.; Wen, Z.H.; Li, B.; Zhang, H.T. The influence of long-time water intrusion on the mineral and pore structure of coal. *Fuel* **2021**, *290*, 119848. [CrossRef]
15. Chen, L.; Zhang, B.M.; Chen, X.H.; Jiang, S.; Zhang, G.T.; Lin, W.B.; Chen, P.; Liu, Z.H. Depositional environment and organic matter accumulation of the Lower Cambrian Shuijingtuo Formation in the middle Yangtze area, China. *J. Pet. Sci. Eng.* **2022**, *208*, 109339. [CrossRef]
16. Hou, H.H.; Shao, L.Y.; Li, Y.H.; Liu, L.; Liang, G.D.; Zhang, W.L.; Wang, X.T.; Wang, W.C. Effect of paleoclimate and paleoenvironment on organic matter accumulation in lacustrine shale: Constraints from lithofacies and element geochemistry in the northern Qaidam Basin, NW China. *J. Pet. Sci. Eng.* **2022**, *208*, 109350. [CrossRef]
17. Sageman, B.B.; Murphy, A.E.; Werne, J.P.; Ver Straeten, C.A.; Hollander, D.J.; Lyons, T.W. A tale of shales: The relative roles of production, decomposition, and dilution in the accumulation of organic-rich strata, Middle-Upper Devonian, Appalachian basin. *Chem. Geol.* **2003**, *195*, 229–273. [CrossRef]
18. Xu, C.; Shan, X.L.; He, W.T.; Zhang, K.; Rexiti, Y.K.; Su, S.Y.; Liang, C.; Zou, X.T. The influence of paleoclimate and a marine transgression event on organic matter accumulation in lacustrine black shales from the Late Cretaceous, southern Songliao Basin, Northeast China. *Int. J. Coal Geol.* **2021**, *246*, 103842. [CrossRef]
19. Zhao, B.S.; Li, R.X.; Qin, X.L.; Wang, N.; Zhou, W.; Khaled, A.; Zhao, D.; Zhang, Y.N.; Wu, X.L.; Liu, Q. Geochemical characteristics and mechanism of organic matter accumulation of marine-continental transitional shale of the lower permian Shanxi Formation, southeastern Ordos Basin, north China. *J. Pet. Sci. Eng.* **2021**, *205*, 108815. [CrossRef]
20. Gao, P.; Li, S.J.; Lash, G.G.; Yan, D.T.; Zhou, Q.; Xiao, X.M. Stratigraphic framework, redox history, and organic matter accumulation of an Early Cambrian intraplatfrom basin on the Yangtze Platform, South China. *Mar. Pet. Geol.* **2021**, *130*, 105095. [CrossRef]
21. Mansour, A.; Wagreich, M. Earth system changes during the cooling greenhouse phase of the Late Cretaceous: Coniacian-Santonian OAE3 subevents and fundamental variations in organic carbon deposition. *Earth Sci. Rev.* **2022**, *229*, 104022. [CrossRef]
22. Ingall, E.D.; Bustin, R.M.; Van Cappellen, P. Influence of water column anoxia on the burial and preservation of carbon and phosphorus in marine shales. *Geochim. Cosmochim. Acta* **1993**, *57*, 303–316. [CrossRef]
23. Yeasmin, R.; Chen, D.Z.; Fu, Y.; Wang, J.G.; Guo, Z.H.; Guo, C. Climatic-oceanic forcing on the organic accumulation across the shelf during the early cambrian (age 2 through 3) in the mid-upper yangtze block, NE guizhou, south China. *J. Asian Earth Sci.* **2017**, *134*, 365–386. [CrossRef]

24. Chen, D.; Wang, J.; Qing, H.; Yan, D.; Li, R. Hydrothermal venting activities in the Early Cambrian, South China: Petrological, geochronological and stable isotopic constraints. *Chem. Geol.* **2009**, *258*, 168.e181. [CrossRef]
25. Wei, H.; Feng, Q.; Yu, J.; Chang, S. Characteristics and Sources of Organic Matter from the Early Cambrian Niutitang Formtion and Its Preservation Environment in Guizhou. *J. Earth Sci.* **2022**, *33*, 933–944. [CrossRef]
26. Guo, Q.J.; Shields, G.A.; Liu, C.Q.; Strauss, H.; Zhu, M.Y.; Pi, D.H.; Goldberg, T.; Yang, X.L. Trace element chemostratigraphy of two Ediacarane-Cambrian successions in South China: Implications for organosedimentary metal enrichment and silicification in the early Cambrian. *Palaeogeogr. Palaeoclimatol. Palaeoecol.* **2007**, *254*, 194.e216. [CrossRef]
27. Guo, Q.; Strauss, H.; Liu, C.; Goldberg, T.; Zhu, M.; Heubeck, C.; Pi, D.; Vernhet, E.; Yang, X.; Fu, P. Carbon isotopic evolution of the terminal Neoproterozoic and Early Cambrian: Evidence from the Yangtze Platform, South China. *Palaeogeogr. Palaeoclimatol. Palaeoecol.* **2007**, *254*, 140.e157. [CrossRef]
28. Liu, Z.H.; Zhuang, X.G.; Teng, G.E.; Xie, X.M.; Yin, L.M.; Bian, L.Z.; Feng, Q.L.; Algeo, T.J. The Lower Cambrian Niutitang Formation at Yangtiao (Guizhou, SW China): Organic matter enrichment, source rock potential, and hydrothermal influences. *J. Pet. Geol.* **2015**, *38*, 411–432. [CrossRef]
29. Liu, K.; Feng, Q.; Shen, J.; Khan, M.; Planavsky, N.J. Increased productivity as a primary driver of marine anoxia in the Lower Cambrian. *Palaeogeogr. Palaeoclimatol. Palaeoecol.* **2018**, *491*, 1–9. [CrossRef]
30. Zhang, Y.; He, Z.; Jiang, S.; Gao, B.; Liu, Z.; Han, B.; Wang, H. Marine redox stratification during the early Cambrian (ca. 529-509 Ma) and its control on the development of organic-rich shales in Yangtze Platform. *Geochem. Geophys. Geosyst.* **2017**, *18*, 2354–2369. [CrossRef]
31. Jin, C.; Li, C.; Algeo, T.J.; Wu, S.; Cheng, M.; Zhang, Z.; Shi, W. Controls on organic matter accumulation on the early-Cambrian western Yangtze Platform, South China. *Mar. Pet. Geol.* **2020**, *111*, 75–87. [CrossRef]
32. Liu, Z.; Yan, D.; Yuan, D.; Niu, X.; Fu, H. Multiple controls on the organic matter accumulation in early Cambrian marine black shales, middle Yangtze Block, South China. *J. Nat. Gas Sci. Eng.* **2022**, *100*, 104454. [CrossRef]
33. Xia, W.; Yu, B.; Sun, M. Depositional settings and enrichment mechanism of organic matter of the black shales at the bottom of Niutitang Formation, lower Cambrian in Southeast Chongqing: A case study from Well Yuke 1. *Acta Geol. Sin-Engl. Ed.* **2015**, *89*, 287. [CrossRef]
34. Wu, Y.W.; Tian, H.; Gong, D.J.; Li, T.F.; Zhou, Q. Paleo-environmental variation and its control on organic matter enrichment of black shales from shallow shelf to slope regions on the Upper Yangtze Platform during Cambrian Stage 3. *Palaeogeogr. Palaeoclimatol. Palaeoecol.* **2020**, *545*, 109653. [CrossRef]
35. Li, J.H.; Wang, H.H.; Li, W.B.; Zhou, X.B. Discussion on global tectonics evolution from plate reconstruction in Phanerozoic. *Acta Pet Sin.* **2014**, *35*, 207–218.
36. Liu, S.; Jin, S.; Liu, Y.; Chen, A. Astronomical forced sequence infill of Early Cambrian Qiongzhusi organic-rich shale of Sichuan Basin, South China. *Sediment. Geol.* **2022**, *440*, 106261. [CrossRef]
37. Zou, C.; Yang, Z.; Dai, J.; Dong, D.; Zhang, B.; Wang, Y.; Deng, S.; Huang, J.; Liu, K.; Yang, C.; et al. The characteristics and significance of conventional and unconventional Sinian–Silurian gas systems in the Sichuan Basin, central China. *Mar. Pet. Geol.* **2015**, *64*, 386–402. [CrossRef]
38. Kokkinos, N.C.; Nkagbu, D.C.; Marmanis, D.I.; Dermentzis, K.I.; Maliaris, G. Evolution of Unconventional Hydrocarbons: Past, Present, Future and Environmental FootPrint. *J. Eng. Sci. Technol. Rev.* **2022**, *15*, 15–24. [CrossRef]
39. Jin, C.; Li, C.; Algeo, T.J.; Planavsky, N.J.; Cui, H.; Yang, X.; Zhao, Y.; Zhang, X.; Xie, S. A highly redox-heterogeneous ocean in South China during the early Cambrian (~529–514 Ma): Implications for biota-environment co-evolution. *Earth Planet Sci. Lett.* **2016**, *441*, 38–51. [CrossRef]
40. Wang, S.; Zou, C.; Dong, D.; Wang, Y.; Li, X.; Huang, J.; Guan, Q. Multiple controls on the paleoenvironment of the Early Cambrian marine black shales in the Sichuan Basin, SW China: Geochemical and organic carbon isotopic evidence. *Mar. Pet. Geol.* **2015**, *66*, 660–672. [CrossRef]
41. Wang, N.; Wen, L.; Li, M.; Dai, X.; Xu, Y.; Ming, Y.; Yang, S. The origin of abnormally $^{13}$C-depleted organic carbon isotope signatures in the early Cambrian Yangtze Platform. *Mar. Pet. Geol.* **2021**, *128*, 105051. [CrossRef]
42. Wang, N.; Li, M.J.; Tian, X.W.; Hong, H.T.; Wen, L.; Wang, W.Z. Climate-ocean control on the depositional watermass conditions and organic matter enrichment in Lower Cambrian black shale in the upper Yangtze Platform. *Mar. Pet. Geol.* **2020**, *120*, 104570. [CrossRef]
43. Wang, J.; Li, Z.X. History of Neoproterozoic rift basins in South China: Implications for Rodinia break-up. *Precambrian Res.* **2003**, *122*, 141–158. [CrossRef]
44. Charvet, J. The Neoproterozoic-Early Paleozoic tectonic evolution of the South China Block: An overview. *J. Asian Earth Sci.* **2013**, *74*, 198–209. [CrossRef]
45. Steiner, M.; Li, G.; Qian, Y.; Zhu, M.; Erdtmann, B.D. Neoproterozoic to Early Cambrian small shelly fossil assemblages and a revised biostratigraphic correlation of the Yangtze Platform (China). *Palaeogeogr. Palaeoclimatol. Palaeoecol.* **2007**, *254*, 67–99. [CrossRef]
46. Gao, P.; Liu, G.; Jia, C.; Young, A.; Wang, Z.; Wang, T.; Zhang, P.; Wang, D. Redox variations and organic matter accumulation on the Yangtze carbonate platform during Late Ediacaran–Early Cambrian: Constraints from petrology and geochemistry. *Palaeogeogr. Palaeoclimatol. Palaeoecol.* **2016**, *450*, 91–110. [CrossRef]
47. Wang, Z.; Jiang, H.; Wang, T.; Lu, W.; Gu, Z.; Xu, A.; Yang, Y.; Xu, Z. Paleo-geomorphology formed during Tongwan tectonization in Sichuan Basin and its significance for hydrocarbon accumulation. *Pet. Explor. Dev.* **2014**, *41*, 338–345. [CrossRef]

48. Li, S.; Gao, P.; Huang, B.; Wang, H.; Wo, Y. Sedimentary constraints on the tectonic evolution of Mianyang-Chang trough in the Sichuan Basin. *Oil Gas Geol.* **2018**, *39*, 889–898.
49. Zhu, M.Y.; Zhang, J.M.; Steiner, M.; Yang, A.H.; Li, G.X.; Erdtmann, B.D. Sinian-Cambrian stratigraphic framework for shallow-to deep-water environments of the Yangtze Platform: An integrated approach. *Prog. Nat. Sci.* **2003**, *13*, 951–960. [CrossRef]
50. Liu, S.; Wang, Y.; Sun, W.; Zhong, Y.; Hong, H.; Deng, B.; Xia, M.; Song, J.; Wen, Y.; Wu, J. Control of intracratonic sags on the hydrocarbon accumulations in the Marine Strata across the Sichuan Basin. *J. Chengdu Univ. of Technol.* **2016**, *43*, 1–23.
51. Du, J.; Wang, Z.; Zou, C.; Xu, C.; Shen, P.; Zhang, B.; Jiang, H.; Huang, S. Discovery of intracratonic rift in the Upper Yangtze and its control effect on the formation of Anyue giant gas field. *Acta Pet Sin.* **2016**, *37*, 1–16.
52. Zhao, J.H.; Jin, Z.J.; Hu, Q.H.; Liu, K.Y.; Liu, G.X.; Gao, B.; Liu, Z.B.; Zhang, Y.Y.; Wang, R.Y. Geological controls on the accumulation of shale gas: A case study of the early Cambrian shale in the Upper Yangtze area. *Mar. Pet. Geol.* **2019**, *107*, 426–437. [CrossRef]
53. Xu, L.; Lehmann, B.; Mao, J.; Qu, W.; Du, A. Re-Os age of polymetallic Ni-Mo-PGE-Au mineralization in early Cambrian black shales of South China—A reassessment. *Econ. Geol.* **2011**, *106*, 511–522. [CrossRef]
54. Yang, C. High Precision Geochronology of the Upper Ediacaran-Lower Cambrian in South China. Ph.D. Thesis, University of Chinese Academy of Sciences, Beijing, China, 2017. (In Chinese).
55. Liang, F.; Jiang, W.; Dai, B.; Chen, Y.; Luo, C.; Zhang, Q.; Tong, K.L.; Hu, X.; Lu, B. Enrichment law and resource potential of shale gas of Qiongzhusi Formation in Weiyuan-Ziyang area. *Nat. Gas. Geosci.* **2022**, *33*, 755–763.
56. Pan, X.Q.; Dong, X.X.; Dai, Q.K.; Luo, J.Z.; Liu, Z.W.; Wang, T.; Hua, H. Fossil assemblages and stratigraphic correlation of the Early Cambrian Jiulaodong Formation in Jinyan-Qianwei Area, Sichuan Basin. *Acta Micropaleontol. Sin.* **2021**, *38*, 241–256. [CrossRef]
57. Liu, J.; Zhang, K.Y. Characteristics of high-resolution stratigraphic sequence of Maidiping Formation and Qiongzhusi Formation in Jingyan area, Sichuan, China. *J. Chengdu Univ. Technol.* **2018**, *45*, 585–593.
58. Zhao, L.K.; Li, W.H.; He, Y.; Zhou, H.F.; Liu, R.; Li, Y.; Wang, W.; Zhong, Y.; Wang, Y.Y. Sedimentation and filling laws of Maidiping-Qiongzhusi formations in Sichuan Basin and their significance of oil and gas geological exploration. *Nat. Gas. Explor. Dev.* **2020**, *43*, 30–38.
59. Lawrence, M.G.; Greig, A.; Collerson, K.D.; Kamber, B.S. Rare earth element and yttrium variability in South East Queensland waterways. *Aquat. Geochem.* **2006**, *12*, 39–72. [CrossRef]
60. Taylor, S.R.; McLennan, S.M. *The Continental Crust: Its Composition and Evolution*; Blackwell Scientific Publications: Oxford, UK, 1985; p. 311.
61. Li, J.; Liang, X.R.; Zhong, L.F.; Wang, X.C.; Ren, Z.Y.; Sun, S.L.; Zhang, Z.F.; Xu, J.F. Measurement of the isotopic composition of molybdenum in geological samples by MC-ICP-MS using a novel chromatographic extraction technique. *Geostand. Geoanal. Res.* **2014**, *38*, 345–354. [CrossRef]
62. Siebert, C.; Nägler, T.F.; Kramers, J.D. Determination of molybdenum isotope fractionation by double-spike multicollector inductively coupled plasma mass spectrometry. *Geochem. Geophys. Geosyst.* **2001**, *2*, 1032. [CrossRef]
63. Zhao, P.P.; Li, J.; Zhang, L.; Wang, Z.B.; Kong, D.X.; Ma, J.L. Molybdenum mass fractions and isotopic compositions of International Geological Reference Materials. *Geostand. Geoanal. Res.* **2016**, *40*, 217–226. [CrossRef]
64. Greber, N.D.; Siebert, C.; Nägler, T.F.; Pettke, T. $\delta^{98/95}$Mo values and molybdenum concentration data for NIST SRM 610, 612 and 3134: Towards a common protocol for reporting Mo data. *Geostand. Geoanal. Res.* **2012**, *36*, 291–300. [CrossRef]
65. Yin, L.; Li, J.; Tian, H.; Long, X. Rhenium-osmium and molybdenum isotope systematics of black shales from the Lower Cambrian Niutitang Formation, SW China: Evidence of a well oxygenated ocean at ca. 520 Ma. *Chem. Geol.* **2018**, *499*, 26–42. [CrossRef]
66. Poulson Brucker, R.L.; McManus, J.; Severmann, S.; Berelson, W.M. Molybdenum behavior during early diagenesis: Insights from Mo isotopes. *Geochem. Geophys. Geosyst.* **2009**, *10*, Q06010. [CrossRef]
67. Wen, H.; Fan, H.; Zhang, Y.; Cloquet, C.; Carignan, J. Reconstruction of early Cambrian ocean chemistry from Mo isotopes. *Geochim. Cosmochim. Acta* **2015**, *164*, 1–16. [CrossRef]
68. Wu, Y.W.; Tian, H.; Li, J.; Li, T.F.; Ji, S. Reconstruction of oceanic redox structures during the Ediacaran-Cambrian transition in the Yangtze Block of South China: Implications from Mo isotopes and trace elements. *Precambrian Res.* **2021**, *359*, 106181. [CrossRef]
69. Dahl, T.W.; Canfield, D.E.; Rosing, M.T.; Frei, R.E.; Gordon, G.W.; Knoll, A.H.; Anbar, A.D. Molybdenum evidence for expansive sulfidic water masses in similar to 750 Ma oceans. *Earth Planet Sci. Lett.* **2011**, *311*, 264–274. [CrossRef]
70. Hatch, J.R.; Leventhal, J.S. Relationship between inferred redox potential of the depositional environment and geochemistry of the Upper Pennsylvanian (Missourian) stark shale member of the Dennis Limestone, Wabaunsee County, Kansas, USA. *Chem. Geol.* **1992**, *99*, 65.e82. [CrossRef]
71. Jones, B.; Manning, D.A. Comparison of geochemical indices used for the interpretation of palaeoredox conditions in ancient mudstones. *Chem. Geol.* **1994**, *111*, 111–129. [CrossRef]
72. Rimmer, S.M.; Thompson, J.A.; Goodnight, S.A.; Robl, T.L. Multiple controls on the preservation of organic matter in Devonian–Mississippian marine black shales: Geochemical and petrographic evidence. *Paleogeogr. Paleoclimatol. Paleoecol.* **2004**, *215*, 125–154. [CrossRef]
73. Algeo, T.J.; Li, C. Redox classification and calibration of redox thresholds in sedimentary systems. *Geochim. Cosmochim. Acta* **2020**, *287*, 8–26. [CrossRef]
74. Qiu, Z.; Tao, H.; Lu, B.; Chen, Z.; Wu, S.; Liu, H.; Qiu, J. Controlling Factors on Organic Matter Accumulation of Marine Shale across the Ordovician-Silurian Transition in South China: Constraints from Trace-Element Geochemistry. *J. Earth Sci.* **2021**, *32*, 887–900. [CrossRef]

75. Ruebsam, W.; Dickson, A.J.; Hoyer, E.M.; Schwark, L. Multiproxy reconstruction of oceanographic conditions in the southern epeiric Kupferschiefer Sea (Late Permian) based on redox-sensitive trace elements, molybdenum isotopes and biomarkers. *Gondwana Res.* **2017**, *44*, 205–218. [CrossRef]
76. Liu, J.S.; Algeo, T.J. Beyond redox: Control of trace-metal enrichment in anoxic marine facies by watermass chemistry and sedimentation rate. *Geochim. Cosmochim. Acta* **2020**, *7*, 296–317. [CrossRef]
77. Algeo, T.J.; Tribovillard, N. Environmental analysis of paleoceanographic systems based on molybdenum–uranium covariation. *Chem. Geol.* **2009**, *268*, 211–225. [CrossRef]
78. Tribovillard, N.; Algeo, T.J.; Baudin, F.; Riboulleau, A. Analysis of marine environmental conditions based on molybdenum–uranium covariation—Applications to Mesozoic paleoceanography. *Chem. Geol.* **2012**, *324–325*, 46–58. [CrossRef]
79. Algeo, T.J.; Lyons, T.W.; Blakey, R.C.; Over, D.J. Hydrographic conditions of the Devono–Carboniferous North American Seaway inferred from sedimentary Mo–TOC relationships. *Palaeogeogr. Palaeoclimatol. Palaeoecol.* **2007**, *256*, 204–230. [CrossRef]
80. Calvert, S.; Pedersen, T. Geochemistry of recent oxic and anoxic marine sediments: Implications for the geological record. *Mar. Geol.* **1993**, *113*, 67–88. [CrossRef]
81. Algeo, T.J.; Lyons, T.W. Mo–total organic carbon covariation in modern anoxic marine environments: Implications for analysis of paleoredox and paleohydrographic conditions. *Paleoceanogr. Paleoclimatol.* **2006**, *21*, PA1016. [CrossRef]
82. Algeo, T.J.; Maynard, J.B. Trace-metal covariation as a guide to water-mass conditions in ancient anoxic marine environments. *Geosphere* **2008**, *4*, 872–887. [CrossRef]
83. Algeo, T.J.; Maynard, J.B. Trace-element behavior and redox facies in core shales of Upper Pennsylvanian Kansas-type cyclothems. *Chem. Geol.* **2004**, *206*, 289–318. [CrossRef]
84. Wang, X.; Shi, X.; Zhao, X.; Tang, D. Increase of seawater Mo inventory and ocean oxygenation during the early Cambrian. *Palaeogeogr. Palaeoclimatol. Palaeoecol.* **2015**, *440*, 621–631. [CrossRef]
85. Xiang, L.; Schoepfer, S.D.; Shen, S.Z.; Cao, C.Q.; Zhang, H. Evolution of oceanic molybdenum and uranium reservoir size around the Ediacaran-Cambrian transition: Evidence from western Zhejiang, South China. *Earth Planet. Sci. Lett.* **2017**, *464*, 84–94. [CrossRef]
86. Zhu, G.; Li, T.; Zhao, K.; Li, C.; Cheng, M.; Chen, W.; Yan, H.; Zhang, Z.; Algeo, T.J. Mo isotope records from Lower Cambrian black shales, northwestern Tarim Basin (China): Implications for the early Cambrian ocean. *Geol. Soc. Am. Bull.* **2022**, *134*, 3–14. [CrossRef]
87. Cheng, M.; Li, C.; Zhou, L.; Algeo, T.J.; Zhang, F.; Romaniello, S.; Jin, C.S.; Lei, L.D.; Feng, L.J.; Jiang, S.Y. Marine Mo biogeochemistry in the context of dynamically euxinic mid-depth waters: A case study of the lower Cambrian Niutitang shales, South China. *Geochim. Cosmochim. Acta* **2016**, *183*, 79–93. [CrossRef]
88. Siebert, C.; Nägler, T.F.; von Blanckenburg, F.; Kramers, J.D. Molybdenum isotope records as a potential new proxy for paleoceanography. *Earth Planet. Sci. Lett.* **2003**, *211*, 159–171. [CrossRef]
89. Wille, M.; Kramers, J.D.; Nägler, T.F.; Beukes, N.J.; Schröder, S.; Meisel, T.; Lacassie, J.P.; Voegelin, A.R. Evidence for a gradual rise of oxygen between 2.6 and 2.5 Ga from Mo isotopes and Re-PGE signatures in shales. *Geochim. Cosmochim. Acta* **2007**, *71*, 2417–2435. [CrossRef]
90. Dahl, T.W.; Anbar, A.D.; Gordon, G.W.; Rosing, M.T.; Frei, R.; Canfield, D.E. The behavior of molybdenum and its isotopes across the chemocline and in the sediments of sulfidic Lake Cadagno, Switzerland. *Geochim. Cosmochim. Acta* **2010**, *74*, 144–163. [CrossRef]
91. Kendall, B.; Komiya, T.; Lyons, T.W.; Bates, S.M.; Gordon, G.W.; Romaniello, S.J.; Jiang, G.; Creaser, R.A.; Xiao, S.; McFadden, K.; et al. Uranium and molybdenum isotope evidence for an episode of widespread ocean oxygenation during the late Ediacaran Period. *Geochim. Cosmochim. Acta* **2015**, *156*, 173–193. [CrossRef]
92. Barling, J.; Arnold, G.L.; Anbar, A.D. Natural mass-dependent variations in the isotopic composition of molybdenum. *Earth Planet. Sci. Lett.* **2001**, *193*, 447–457. [CrossRef]
93. Goldberg, T.; Archer, C.; Vance, D.; Poulton, S.W. Mo isotope fractionation during adsorption to Fe (oxyhydr) oxides. *Geochim. Cosmochim. Acta* **2009**, *73*, 6502–6516. [CrossRef]
94. Neubert, N.; Nägler, T.F.; Böttcher, M.E. Sulfidity controls molybdenum isotope fractionation into euxinic sediments: Evidence from the modern Black Sea. *Geology* **2008**, *36*, 775–778. [CrossRef]
95. Helz, G.R.; Miller, C.V.; Charnock, J.M.; Mosselmans, J.F.W.; Pattrick, R.A.D.; Garner, C.D.; Vaughan, D.J. Mechanism of molybdenum removal from the sea and its concentration in black shales: EXAFS evidence. *Geochim. Cosmochim. Acta* **1996**, *60*, 3631–3642. [CrossRef]
96. Barling, J.; Anbar, A.D. Molybdenum isotope fractionation during adsorption by manganese oxides. *Earth Planet. Sci. Lett.* **2004**, *217*, 315–329. [CrossRef]
97. Scholz, F.; McManus, J.; Sommer, S. The manganese and iron shuttle in a modern euxinic basin and implications for molybdenum cycling at euxinic ocean margins. *Chem. Geol.* **2013**, *355*, 56–68. [CrossRef]
98. Ostrander, C.M.; Kendall, B.; Olson, S.L.; Lyons, T.W.; Gordon, G.W.; Romaniello, S.J.; Zheng, W.; Reinhard, C.T.; Roy, M.; Anbar, A.D. An expanded shale $\delta^{98}$Mo record permits recurrent shallow marine oxygenation during the Neoarchean. *Chem. Geol.* **2020**, *532*, 119391. [CrossRef]
99. Arnold, G.L.; Anbar, A.D.; Barling, J.; Lyons, T.W. Molybdenum isotope evidence for widespread anoxia in mid-proterozoic oceans. *Science* **2004**, *304*, 87–90. [CrossRef] [PubMed]
100. Chen, X.; Ling, H.F.; Vance, D.; Shields-Zhou, G.A.; Zhu, M.; Poulton, S.W.; Och, L.M.; Jiang, S.Y.; Li, D.; Cremonese, L.; et al. Rise to modern levels of ocean oxygenation coincided with the Cambrian radiation of animals. *Nat. Commun.* **2015**, *6*, 7142. [CrossRef]

101. Xu, L.; Lehmann, B.; Mao, J.; Nägler, T.F.; Neubert, N.; Böttcher, M.E.; Escher, P. Mo isotope and trace element patterns of Lower Cambrian black shales in South China: Multi-proxy constraints on the paleoenvironment. *Chem. Geol.* **2012**, *318–319*, 45–59. [CrossRef]
102. Paytan, A.; Griffith, E.M. Marine barite: Recorder of variations in ocean export productivity. *Deep Sea Res. Part II Top. Stud. Oceanogr.* **2007**, *54*, 687–705. [CrossRef]
103. Tribovillard, N.; Algeo, T.J.; Lyons, T.; Riboulleau, A. Trace metals as paleoredox and paleoproductivity proxies: An update. *Chem. Geol.* **2006**, *232*, 12–32. [CrossRef]
104. Little, S.; Vance, D.; Lyons, T.; McManus, J. Controls on trace metal authigenic enrichment in reducing sediments: Insights from modern oxygen-deficient settings. *Am. J. Sci.* **2015**, *315*, 77–119. [CrossRef]
105. Xu, D.T.; Wang, X.Q.; Shi, X.Y.; Tang, D.J.; Zhao, X.K.; Feng, L.J.; Song, H.Y. Nitrogen cycle perturbations linked to metazoan diversification during the early Cambrian. *Palaeogeogr. Palaeoclimatol. Palaeoecol.* **2020**, *538*, 109392. [CrossRef]
106. Schoepfer, S.D.; Shen, J.; Wei, H.; Tyson, R.V.; Ingall, E.; Algeo, T.J. Total organic carbon, organic phosphorus, and biogenic barium fluxes as proxies for paleomarine productivity. *Earth Sci. Rev.* **2015**, *149*, 23–52. [CrossRef]
107. Xia, P.; Hao, F.; Tian, J.; Zhou, W.; Fu, Y.; Guo, C.; Yang, Z.; Li, K.; Wang, K. Depositional Environment and Organic Matter Enrichment of Early Cambrian Niutitang Black Shales in the Upper Yangtze Region, China. *Energies* **2022**, *15*, 4551. [CrossRef]
108. Sweere, T.; van den Boorn, S.; Dickson, A.J.; Reichart, G.J. Definition of new trace-metal proxies for the controls on organic matter enrichment in marine sediments based on Mn, Co, Mo and Cd concentrations. *Chem. Geol.* **2016**, *441*, 235–245. [CrossRef]
109. Cremonese, L.; Shields-Zhou, G.; Struck, U.; Ling, H.F.; Och, L.; Chen, X.; Li, D. Marine biogeochemical cycling during the early Cambrian constrained by a nitrogen and organic carbon isotope study of the Xiaotan section, South China. *Precambrian Res.* **2013**, *225*, 148–165. [CrossRef]
110. Yuan, Y.; Cai, C.; Wang, T.; Xiang, L.; Jia, L.; Chen, Y. Redox condition during Ediacaran-Cambrian transition in the Lower Yangtze deep water basin, South China: Constraints from iron speciation and $\delta^{13}C_{org}$ in the Diben section, Zhejiang. *Chin. Sci. Bull.* **2014**, *59*, 3638–3649. [CrossRef]
111. Gao, P.; He, Z.L.; Li, S.J.; Lash, G.G.; Li, B.; Huang, B.Y.; Yan, D.T. Volcanic and hydrothermal activities recorded in phosphate nodules from the Lower Cambrian Niutitang Formation black shales in South China. *Palaeogeogr. Palaeoclimatol. Palaeoecol.* **2018**, *505*, 381–397. [CrossRef]
112. He, T.H.; Lu, S.F.; Li, W.H.; Sun, D.Q.; Pan, W.Q.; Zhang, B.S.; Tan, Z.Z.; Ying, J.F. Paleoweathering, hydrothermal activity and organic matter enrichment during the formation of earliest Cambrian black strata in the Paleo-environmental variation and its control on organic matter enrichment of black shales from shallow shelf to slope regions on the Upper Yangtze Platform during Cambrian Stage 3e northwest Tarim Basin, China. *J. Pet. Sci. Eng.* **2020**, *545*, 106987. [CrossRef]
113. Ma, Y.Q.; Fan, M.J.; Lu, Y.C.; Liu, H.M.; Hao, Y.Q.; Xie, Z.H.; Liu, Z.H.; Peng, L.; Du, X.B.; Hu, H.Y. Climate-driven paleolimnological change controls lacustrine mudstone depositional process and organic matter accumulation: Constraints from lithofacies and geochemical studies in the Zhanhua Depression, eastern China. *Int. J. Coal Geol.* **2016**, *167*, 103–118. [CrossRef]
114. Tyson, R.V. Sedimentation rate, dilution, preservation and total organic carbon: Some results of a modelling study. *Org. Geochem.* **2001**, *32*, 333–339. [CrossRef]
115. Mansour, A.; Wagreich, M.; Gentzis, T.; Ocubalidet, S.; Tahoun, S.S.; Elewa, A.M. Depositional and organic carbon-controlled regimes during the Coniacian-Santonian event: First results from the southern Tethys (Egypt). *Mar. Pet. Geol.* **2020**, *115*, 104285. [CrossRef]
116. Pedersen, T.; Calvert, S. Anoxia vs. productivity: What controls the formation of organic-carbon-rich sediments and sedimentary Rocks. *AAPG Bull.* **1990**, *74*, 454–466.
117. Dong, T.; Harris, N.B.; Ayranci, K. Relative sea-level cycles and organic matter accumulation in shales of the Middle and Upper Devonian Horn River Group, northeastern British Columbia, Canada: Insights into sediment flux, redox conditions, and bioproductivity. *Geol. Soc. Am. Bull.* **2018**, *130*, 859–880. [CrossRef]
118. Yarincik, K.M.; Murray, R.W.; Peterson, L.C. Climatically sensitive eolian and hemipelagic deposits in the Cariaco Basin, Venezuela, over past 578,000 years: Results from Al/Ti and K/Al. *Paleoceanography* **2000**, *15*, 210–228. [CrossRef]
119. Beckmann, B.; Flögel, S.; Hofmann, P.; Schulz, M.; Wagner, T. Orbital forcing of Cretaceous river discharge in tropical Africa and ocean response. *Nature* **2005**, *437*, 241–244. [CrossRef] [PubMed]